CONDENSED MATTER PHYSICS

Room temperature coherent control of spin defects in hexagonal boron nitride

Andreas Gottscholl[1], Matthias Diez[1], Victor Soltamov[1], Christian Kasper[1], Andreas Sperlich[1], Mehran Kianinia[2], Carlo Bradac[3], Igor Aharonovich[2,4], Vladimir Dyakonov[1]*

Optically active spin defects are promising candidates for solid-state quantum information and sensing applications. To use these defects in quantum applications coherent manipulation of their spin state is required. Here, we realize coherent control of ensembles of boron vacancy centers in hexagonal boron nitride (hBN). Specifically, by applying pulsed spin resonance protocols, we measure a spin-lattice relaxation time of 18 microseconds and a spin coherence time of 2 microseconds at room temperature. The spin-lattice relaxation time increases by three orders of magnitude at cryogenic temperature. By applying a method to decouple the spin state from its inhomogeneous nuclear environment the optically detected magnetic resonance linewidth is substantially reduced to several tens of kilohertz. Our results are important for the employment of van der Waals materials for quantum technologies, specifically in the context of high resolution quantum sensing of two-dimensional heterostructures, nanoscale devices, and emerging atomically thin magnets.

INTRODUCTION

Van der Waals (vdW) crystals have recently emerged as a promising family of materials to investigate light matter interaction at the nanoscale (*1*–*4*). Out of a growing suite of vdW crystals, hexagonal boron nitride (hBN) stands out owing to its ability to host optically active defects that emit single photons of light while displaying spin-optical quantum properties at room temperature (*5*, *6*). A specific defect of interest is the negatively charged boron vacancy (V_B^-) center. This atom-like defect has a spin triplet ground state ($S = 1$) (*7*), which can be prepared, manipulated, and optically read out through a combination of microwave and laser excitation cycles (*6*); a feat that makes it particularly appealing for quantum sensing and spintronic applications. In the realm of vdW heterostructures, having an optically active spin sensor confined in an intrinsically atom-thin, two-dimensional (2D) host is highly desirable, as it allows for achieving high-resolution sensing strategies with specific requirements such as, for instance, imaging the magnetic domains in 2D ferromagnets (*8*–*10*) or magnetic superlattices (*11*).

However, before these defects can be used in practical implementations, full understanding and, ultimately, control of their coherent properties must be acquired. In this work, we demonstrate coherent control of an ensemble of V_B^- defects in hBN. While coherent control of spin qubits in 3D crystals [e.g., diamond, silicon carbide (SiC), or rare earth ions in glass] (*12*–*16*) has been demonstrated, spin defects in vdW crystals are still unexplored. We further show that the coherence properties of V_B^- spin ensembles are influenced by the coupling with the surrounding nuclei spin bath (^{14}N with $I = 1$,^{10}B with $I = 3$, and ^{11}B with $I = {}^3/_2$). By applying optically detected two- and three-pulse electron spin-echo envelope modulation (ESEEM), we were able to probe magnetic and quadrupole fields of surrounding nuclei and obtain information about hyperfine coupling and quadrupole splitting, although an exact assignment to nitrogen or boron in their corresponding coordination shells remains ambiguous. By implementing a two-frequency optically detected magnetic resonance (ODMR) technique to the V_B^- spin system, we demonstrate the ability to selectively saturate one of the hyperfine transitions and effectively decouple the electron spin system from the nuclear bath, which allows estimating the upper limit of the highest achievable coherence times.

RESULTS AND DISCUSSION

A schematic of the V_B^- defect is shown in Fig. 1A. The defect consists of a missing boron atom in the hBN crystal in the negatively-charged state. The corresponding simplified energy level diagram is shown in Fig. 1B. The defect has a nominal D_{3h} symmetry (lower symmetries are expected because of strain and reorganization), and the main optical transition takes place between the $^3E''$ and $^3A'_2$ levels. When excited with a 532-nm laser source, the defect emits at a wavelength centered at ~850 nm. The inset shows the evolution of the $|0\rangle$ substate on the Bloch sphere under the action of the microwave field.

Figure 1C shows the continuous-wave (CW) ODMR spectrum of the V_B^- defects at room temperature. The signal is centered around the 3.5-GHz frequency, corresponding to the zero-field splitting (ZFS). The photoluminescence (PL) intensity signal is frequency dependent. The two distinct features at frequencies ν_1 and ν_2 correspond to the ground-state spin transitions $|0\rangle \leftrightarrow |-1\rangle$ and $|0\rangle \leftrightarrow |+1\rangle$ and occur because the ground $m_s = \pm 1$ states scatter less photons than the $m_s = 0$ state, through the excited state. Both features show a clearly resolved hyperfine splitting with seven peaks due to three equivalent nitrogen nuclei ($2nI + 1 = 7$, with $n = 3$, $I = 1$) in the hBN plane surrounding the missing boron atom. To explain the observed transitions and their variation with the magnetic field, we use the spin Hamiltonian, which describes electron spin-spin interaction (ZFS), electron and nuclear Zeeman

[1]Experimental Physics 6 and Würzburg-Dresden Cluster of Excellence ct.qmat, Julius Maximilian University of Würzburg, 97074 Würzburg, Germany. [2]School of Mathematical and Physical Sciences, University of Technology Sydney, Ultimo, NSW 2007, Australia. [3]Department of Physics and Astronomy, Trent University, 1600 West Bank Dr., Peterborough, ON K9J 0G2, Canada. [4]ARC Centre of Excellence for Transformative Meta-Optical Systems, Faculty of Science, University of Technology Sydney, Ultimo, NSW 2007, Australia.
*Corresponding author. Email: vladimir.dyakonov@uni-wuerzburg.de

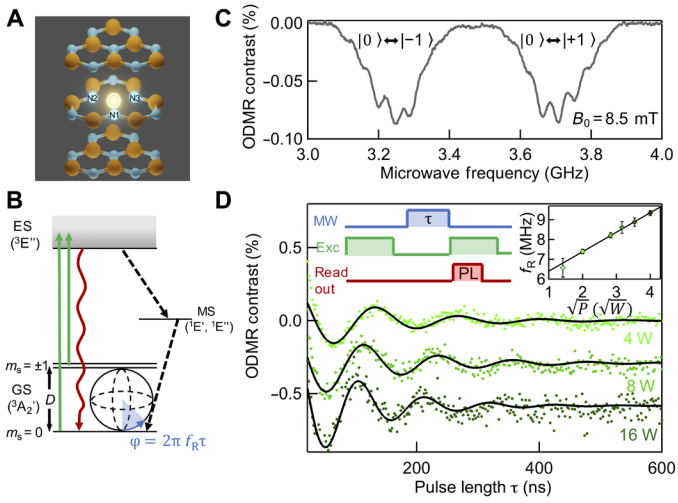

Fig. 1. Coherent manipulation of V_B^- spin centers in hBN at room temperature. (**A**) Schematic of the V_B^- defect in hBN: a negatively charged boron vacancy (bright spot) surrounded by three equivalent nitrogen atoms (blue spheres, N1 to N3). (**B**) V_B^- defect energy diagram and the optical pumping cycle comprising excitation to excited state (ES) (green), radiative recombination (red), and nonradiative decay to ground state (GS) via metastable state (MS) (dashed lines). *D* denotes ZFS. The $|0\rangle\leftrightarrow|-1\rangle$ transition is represented on a Bloch sphere. The ground state $|0\rangle$ is spin polarized by a laser (green) and can be manipulated to an angle φ after applying microwaves with the Rabi frequency f_R for a time τ. (**C**) Continuous-wave (CW) ODMR spectrum with two characteristic transitions in a magnetic field of 8.5 mT. Both signals reveal structure due to hyperfine interaction (HFI) with three next neighboring nitrogen atoms. (**D**) Optically detected Rabi oscillations on transition $|0\rangle\leftrightarrow|-1\rangle$ after initialization into $|0\rangle$ state for different microwave (MW) powers. The inset schematically shows the pulse sequence, in which the first excitation laser pulse (green) is used for the initialization of the spin state and the second one for a readout (red) of the current state after the microwave pulse (blue). Rabi frequency f_R versus square root of microwave power *P*, which is proportional to B_1 field, is also shown.

interaction, electron-nuclear hyperfine interaction (HFI), and electric quadrupole interaction (QI)

$$H = \underbrace{D(S_z^2 - S(S+1)/3) + E(S_x^2 - S_y^2)}_{\text{ZFS}} + \underbrace{g_e \mu_B \mathbf{BS}}_{e\text{–Zeeman}} + \underbrace{\mathbf{SAI}}_{\text{HFI}} + \underbrace{Q(I_z^2 - I(I+1)/3)}_{\text{QI}} - \underbrace{g_N \mu_N \mathbf{BI}}_{n\text{–Zeeman}} \quad (1)$$

where *D* and *E* are the ZFS parameters, *S* is the total electron spin (*S* = 1 for V_B^-), *g* is the Landé factor, μ_B is the Bohr magneton, μ_N is the nuclear magneton, *B* is the static magnetic field, $S_{x,y,z}$ are the spin-1 operators, **A** is the HFI tensor, **I** and I_Z are nuclear operators, and *Q* is the quadrupole coupling constant. The hyperfine coupling constant due to coupling with ^{14}N (*I* = 1) in the first coordination shell *A* = 47 MHz is known from the experiment and confirmed by calculations (*6*, *17*).

To get access to the spin dynamics of the V_B^-, and to determine their spin relaxation times T_1 and T_2, we perform pulsed ODMR measurements. They are based on preparing the ground spin state of the system by optical excitation, applying microwave pulses of variable length to coherently manipulate the spin state, and lastly performing an optical readout of the state. Figure 1D shows Rabi oscillations with a characteristic frequency f_R in the megahertz range, which depends on the microwave power and, hence, the strength of the B_1 component of the microwave field, as shown in the inset. These measurements allow calibrating the microwave pulse length at a given power for subsequent pulsed ODMR experiments.

The upper limit for spin coherence is given by the spin-lattice relaxation time T_1, which we determine with a standard π-pulse sequence (*12*, *13*), as shown in Fig. 2A. The T_1 time is around 18 μs and does not seem to be influenced by an external magnetic field, even if the two ODMR peaks collapse and form a single peak at *B* = 0 (see inset to Fig. 2A). The gray background indicates the overlap of the two transitions ν_1 and ν_2 below 5 mT. This can be explained by the large ZFS compared to the small external magnetic field applied. Note that ZFS of V_B^- centers in hBN is 3.5 GHz and the magnetic fields applied in our experiments are not large enough to induce the level anticrossing (*B* ≈ 125 mT). Hence, the local magnetic field at the spin defect site dominates the spin properties. This leads to a robust spin-lattice relaxation dynamic of the V_B^- defect, independent of external magnetic perturbation fields.

To gain further insights into the nature of spin-lattice relaxation mechanisms, e.g., the interaction with lattice phonons, we probe the temperature dependence of T_1. In this case, one would vary the spectrum of vibronic lattice modes, which are an effective relaxation channel if they have energies comparable to the Larmor frequency of the electron spin. The V_B^- ZFS is very large, so one can expect a relaxation behavior similar to the nitrogen vacancy (NV) centers in diamond, where the direct one-phonon absorption and emission processes are neglected at higher temperatures (*18*). Nevertheless, the 2D character of the hBN and the symmetry of the spin defects are expected to influence their vibronic properties compared to 3D crystals (*19*, *20*), although detailed calculations about these effects in the presence of spin defect or experimental data are not yet available.

To study the behavior of spin-phonon contributions to T_1, we use the pulse sequence shown in Fig. 2A and varied the temperature between 300 and 20 K. Figure 2B reveals a monotonic growth of T_1, as the temperature decreases, up to a value of 12.5 ms at *T* = 20 K. In general, the T_1 time is governed by the following processes (*21*, *22*)

$$\frac{1}{T_1} = A_0 + A_1 T + A_s T^s + \frac{R}{\exp\left(\frac{\Delta}{k_B T}\right) - 1} \quad (2)$$

Single-phonon scattering processes are considered by the linear term A_1. Two-phonon processes (direct transition, Stokes, anti-Stokes, and spontaneous emission) are described by the A_s term (higher orders *s* + 1 and *s* + 2 are neglected), where *s* = 4ν + 2*d* − 3 (*22*). Because *d* is the dimension of the system and ν is a phenomenological spin-phonon coupling factor reflecting the symmetry of the lattice (ν = $^1/_2$ for a noncubic), one expects *s* = 5 for the NV centers in diamond and silicon vacancies (V_{Si}) in SiC. For a noncubic 2D system such as hBN (*d* = 2, ν = $^1/_2$), one expects *s* = 3. Orbach-type processes resulting from quasi-localized phonon modes are described by an exponential contribution with the characteristic energy Δ = ħω$_{loc}$ and its fitting parameter *R* with dimension per second. Therefore, the spin-lattice relaxation rate is ultimately limited by A_0, which provides the longest achievable T_1 time. To quantify the observed temperature dependence shown in Fig. 2B, a double logarithmic scaling of the spin-lattice relaxation rate $1/T_1$ is depicted in the inset. All observed values can be fitted with only one line with a slope of *s* = $^5/_2$ that corresponds to $\frac{1}{T_1} \sim T^{5/2}$. This value differs from the expected values of *s* = 3 (*s* = 5) for a 2D (3D) system mentioned above. Because the experimental values are all in the

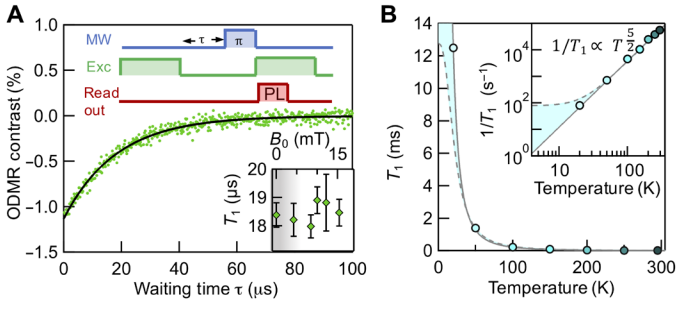

Fig. 2. Spin-lattice relaxation dynamics of V_B^- spin centers in hBN. (**A**) ODMR signal decay with waiting time τ at $T = 300$ K. The pulse sequence is schematically shown, in which the duration of microwave π-pulse is known from Rabi experiments and the waiting time τ is varied. Inset schematically shows T_1 versus external magnetic field (0 to 15 mT). The gray background indicates the magnetic field range where two ODMR transitions ν_1 and ν_2 overlap. (**B**) Temperature dependence of the spin-lattice relaxation time of V_B^- spin centers in hBN. The T_1 time increases by three orders of magnitude from 18 μs to 12.5 ms, when lowering the temperature to 20 K. Inset shows that a log-log plot for the spin-lattice relaxation rate ($1/T_1$) shows a $T^{5/2}$ behavior over a broad temperature range. An upper boundary for the fastest spin-lattice relaxation rate can be estimated by assuming a saturation of the T_1 time at 20 K (highlighted in blue).

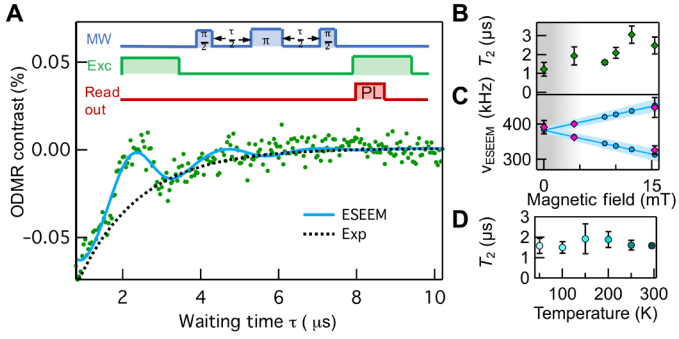

Fig. 3. Spin-spin relaxation dynamics and nuclear modulation effects. (**A**) The applied spin-echo pulsed sequence including the projection pulse π/2 and the ODMR contrast versus waiting time τ (green) is shown. The expected exponential rise (black dotted line) is superimposed by the oscillations (green and blue) due to coupling of electron spins to nuclei. (ESEEM effect, see text). The fit with modulated exponential function (blue) allows estimating the ESEEM frequencies and the T_2 time. (**B**) T_2 time versus magnetic field. T_2 slightly decreases in the magnetic field range where ODMR transitions ν_1 and ν_2 overlap (gray area), indicating the presence of additional decoherence, e.g., due to HFI. (**C**) ESEEM frequency versus external magnetic field. Plotted are frequencies obtained from the two-pulse (blue) and three-pulse (pink) ESEEM. The ESEEM frequency is proportional to the applied magnetic field according to the nuclear Zeeman effect, while the offset is given by a quadrupole splitting due to surrounding nuclei. The error margins two-pulse ESEEM are shown in light blue. (**D**) T_2 time versus temperature. $B = 8.5$ mT.

linear regime (in the log-log scale), it is not possible to make any further assumptions regarding other spin-lattice rate contributions such as linear terms or Orbach-related effects. Nevertheless, an estimate for the lowest relaxation rate corresponding to the longest measured $T_1 = 12.5$ ms can be given. Assuming that the spin-lattice relaxation rate starts to level off and becomes temperature independent at temperatures below 20 K (*13*, *18*, *21*), an upper limit for the term $A_0 < 80\ s^{-1}$ can be set, as highlighted in blue in Fig. 2B.

After determining the T_1 relaxation time, we proceed with T_2 time. The microwave protocol for measuring the Rabi oscillations (Fig. 1D) can also be used to estimate the upper limit of the spin-dephasing time T_2^* induced by surrounding magnetic moments by fitting the Rabi oscillations with the function $f(\tau) = f_0 + A * \exp(-\tau/T_2^*)\cos(2\pi\nu_{Rabi}\tau)$ as $T_2^* = 100$ ns. We then measure the T_2 time of the V_B^- defects with a Hahn spin-echo sequence (*23*–*25*). The pulse sequence applied is π/2-τ-π-τ-echo, and the results are shown in Fig. 3A. Note that to enable optical detection of spin echo, an additional π/2-pulse (*26*–*28*) is required after the standard spin-echo pulse sequence to read out the spin polarization of a well-defined state (bright state $|0\rangle$) versus dark states $|\pm1\rangle$). The ODMR transient shows the exponential rise from which we determine the spin coherence T_2 time. A room temperature spin-spin coherence time of $T_2 \approx 2$ μs can be extracted for an external magnetic field of 8.5 mT.

As shown in Fig. 3B, T_2 increases slightly to about 3 μs by increasing the magnetic field above the region where the ODMR signals overlap (gray zone). Furthermore, the ODMR transient is superimposed by oscillations containing two frequencies, as determined by Fourier analysis and plotted for different magnetic fields in Fig. 3C. The effect is known as ESEEM (*29*) and is widely used to study interactions between electron and nuclear spins. In ESEEM, the electron spin-echo envelope exhibits amplitude modulation that corresponds to the nuclear magnetic resonance (NMR) frequencies of nuclei, which are coupled to the electron spin.

For the V_B^-, only one ESEEM frequency is expected if the HFI of the electron spin with three equivalent nitrogen nuclei ($I = 1$) in the first coordination sphere is considered. For all nuclei with $I > {}^1/_2$, however, the quadrupole term becomes important, as described in Eq. 1 because it modifies the NMR frequency spectrum considerably. In this case, one expects six frequencies derived from the combination of the Zeeman nuclear and the quadrupole splitting of the surrounding nuclei, as shown in fig. S1. Note that additional splitting (with corresponding frequencies) are expected when the ^{10}B ($I = 3$) nuclei are taken into account. Because of experimental limitations, we can only resolve two of them. Figure 3C plots a global fit over all T_2 transients measured at different magnetic fields (blue circles). Additional frequency values for other magnetic fields obtained by three-pulse ESEEM (see fig. S2) are also shown (pink diamonds), and they complement the field dependence obtained by the two-pulse ESEEM within the error margin (shown in light blue). The ESEEM frequencies evolve linearly with the magnetic field B following the law $\nu_{ESEEM} = |\nu_0 \pm \gamma B|$, where $\gamma = 4.54 \pm 0.59$ kHz/mT and $\nu_0 = 382.9 \pm 4.4$ kHz is the frequency at $B = 0$. In the absence of magnetic field, the nuclear Zeeman splitting is zero, and ESEEM arises only from the nuclear QI and/or HFI (*30*) and can be used to determine the quadrupole coupling as $Q = \nu_0 = 383$ kHz (Eq.1), as shown in Fig. 3C. The experimentally derived γ is close to the tabulated value of the ^{10}B nuclear gyromagnetic ratio $[\gamma(^{10}B) = 4.575$ kHz/mT]; thus, the observed oscillations are possibly due to the coherent coupling of the electron spin with the ^{10}B nuclear spin bath. Note that the coupling of the electron spin V_B^- with the neighboring ^{14}N nuclear spin with slightly smaller gamma $[\gamma(^{14}N) = 3.076$ kHz/mT] cannot be fully disregarded because it is also within the error margins of the $\nu_{ESEEM}(B)$ dependence in Fig. 3C. The three nearest ^{14}N nuclei strongly coupled to V_B^- via HFI ($A = 47$ MHz) cannot be excited with the available B_1 field, which is in the range of 0.33 mT because the condition $\gamma_e B_1 > A$, where $\gamma_e = 28$ MHz/mT is not fulfilled, and therefore, they cannot be seen in the modulation pattern of the ESEEM.

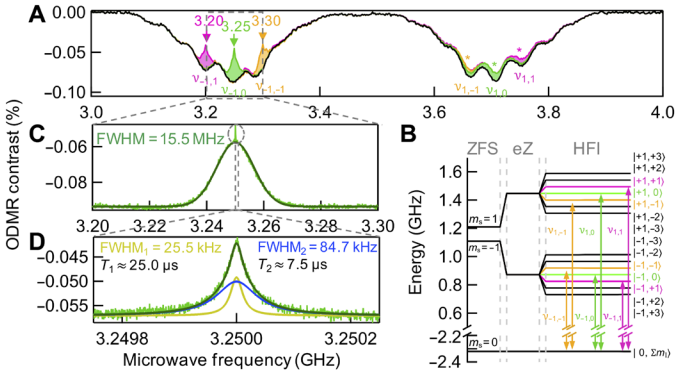

Fig. 4. CW multifrequency ODMR measurements at $T = 300$ K. (**A**) A standard CW ODMR measurement is plotted in black. Applying a second microwave frequency (pump) leads to a dip (hole) indicated by an arrow (3.20 GHz, pink; 3.25 GHz, green; 3.30 GHz, orange). A second peak (indicated by an asterisk) appears symmetrically to the center of the spectrum (3.48 GHz) for the transitions from $m_S = 0$ to $|-1, -1\rangle$ and $|+1, -1\rangle$ substates, respectively. (**B**) Simplified energy diagram illustrating the hyperfine splitting due to three equivalent nitrogen nuclei with the respective electronic and nuclear spin quantum numbers m_S and m_I. (**C**) The hole spectrum. By modulating the fixed (pump) frequency instead of the swept (probe) frequency the pristine hole spectrum can be obtained directly. The signal consists of a broad inhomogeneously broadened Gaussian peak and a very narrow spike on top in the center. (**D**) The narrow peak is due to coherent population oscillations, it consits of two contributions, and can be fitted with two Lorentz functions (yellow and blue, sum of both in green). The inset shows the respective full width at half maximum (FWHM) and the inversed values assigned to spin-relaxation times T_1 and T_2.

A slight increase in the spin coherence time T_2 with increasing magnetic field (Fig. 3B) may be due to the partial suppression of heteronuclear or homonuclear spin pair flip-flop processes (cross-resonances) in a moderate magnetic field (*31*); however, the nuclear spin bath of the hBN lattice with ^{14}N (99.6%) (nuclear spin $I = 1$), ^{11}B (80.1%), and ^{10}B (19.9%) that have nuclear spin of $^3/_2$ and 3, respectively, remains a major factor of decoherence. Observed ESEEM frequencies clearly show that the electron spin of V_B^- is coherently coupled to nuclear spins in the distant coordination shells from the vacancy, but the exact decoherence mechanism is not yet understood.

Figure 3D shows a nearly temperature-independent T_2 when we varied the temperature between 300 and 50 K. This behavior can be attributed to the high defect density in the sample (see fig. S3) together with the smallness of the Boltzmann factor to polarize nuclear and electronic spin systems and, thus, to suppress the decoherence in these magnetic field and temperature ranges and is also reported for NV centers in diamond (*32*) and silicon vacancies in SiC (*28*).

To further explore the origins of the ODMR line broadening and, hence, the spin-dephasing, we apply a two-frequency CW ODMR technique, which eliminates the contributions of the magnetic nuclei. The so-called "hole-burning" technique (*33*–*36*) is realized by introducing a second frequency (pump), which is fixed within the inhomogeneously broadened ODMR line. In Fig. 4A, a standard CW ODMR spectrum is shown (black curve). Applying a second microwave frequency results in a sharp dip in a particular ODMR transition at the position of the applied frequency. This is shown for three selected resonances at 3.2 GHz (pink), 3.25 GHz (green), and 3.3 GHz (orange), respectively. The pump microwave field excites modes in certain spin packets, and if the power is sufficiently high, then it saturates them, resulting in a reduction in ODMR contrast.

To evaluate the spin hole-burning and extract the "hole" spectrum directly, we zoom into a selected transition at 3.25 GHz, as shown in Fig. 3C. The spectral shape of the hole can be fitted by a Gaussian function with a full width at half maximum (FWHM) of 15.5 MHz with a sharp spike in the middle. The linewidth of a broad component is 15.5 MHz and much narrower than the ODMR signal with the linewidth of several hundreds of megahertz due to hyperfine broadening. Thus, by saturating an individual hyperfine transition, we are able to eliminate the linewidth contribution from magnetic nuclei and separate a spin package. As shown in Fig. 4D, a 500-kHz frequency sweep around the center of the hole reveals a spike that is perfectly reproducible by two Lorentz functions with 84.7-kHz (blue) and 25.5-kHz (yellow) linewidths, respectively. This narrow spike can be explained by coherent population oscillations, where the ground-state population of a two-level quantum system oscillates at the beat frequency between the pump and probe (swept frequency) fields (*33*, *34*, *37*). These oscillations can be observed only if the beat frequency is less than, or approximately equal to, the inverse of the population relaxation time.

Projecting the spectral hole-burning in optical spectroscopy to the V_B^- spin system, the width of the spike can be related to the population decay rates (relevant spin-relaxation processes) (*33*, *38*). Because there are two contributions to the linewidth, we assign the narrow contribution (25.5 kHz) to the spin-lattice relaxation rate and extract a T_1^{HB} of 25.0 µs. Consequently, the second contribution (84.7 kHz) is assigned to T_2^{HB} of 7.5 µs. In particular, the spin-spin relaxation time estimated in this way exceeds the value measured directly by pulsed ODMR by a factor of three after the broadening contributions are strongly suppressed by the surrounding nuclear bath and can therefore be regarded as the upper limit for the relaxation rates for V_B^- in hBN at room temperature. Note that the spectral hole is mirrored relative to the ODMR spectrum symmetry axis at $D/h = 3.48$ GHz and also appears in the second ODMR transition (~3.7-GHz range), as indicated by asterisks in Fig. 4A.

To understand this phenomenon, one can use a simplified energy diagram in which only the HFI with three equivalent nitrogen nuclei is considered (see Fig. 4B). (Figure S1 gives a detailed overview of all energy contributions.) As soon as the pump frequency has saturated the transition, e.g., between the $m_S = 0$ state and the $|-1, -1\rangle$ substate of $m_S = -1$ state, the hole in the left (low-frequency) ODMR signal is "burned." Hence, the state $m_S = 0$ is already depleted and is kept so, therefore, the intensity of the transition to the substate $|+1, -1\rangle$ of the state $m_S = +1$ (high-frequency ODMR signal) will also be lower. This applies to all transitions that correspond to the nuclear spin quantum numbers m_I.

To conclude, we demonstrated coherent control of the V_B^- spin ensemble in hBN at room temperature. Our results suggest reasonably long spin-relaxation times $T_1 \approx 18$ µs and $T_2 \approx 2$ µs at room temperature that can be substantially increased to $T_1 \approx 12.5$ ms at cryogenic temperatures. The behavior is governed by spin-phonon interaction and follows a power law of $T^{-5/2}$. Using a spin hole-burning technique, we determine the upper limit of the spin-relaxation times to $T_1^{HB} \approx 25.0$ µs and $T_2^{HB} \approx 7.5$ µs at room temperature by suppressing the inhomogeneous broadening due to the surrounding nuclear bath. In addition, the electronic spin system can be further decoupled from the detrimental nuclear bath, as was demonstrated for other 3D systems (*39*–*41*), whereby the spin

coherence times needs to be seen in relation to other properties depending on the applications (*13*, *42*). The ability to engineer V_B^- defects in thin hBN flakes on demand (*43*) offers promising perspectives for deploying quantum sensing with vdW crystals. For instance, positioning a monolayer or few layer hBN with embedded V_B^- within a stack of 2D materials can provide an in situ magnetometer to sense the surrounding electromagnetic fields (*44*, *45*) or couple the spin to the valley degree of freedom from the surrounding excitons in transition metal dichalcogenides (*46*).

MATERIALS AND METHODS

hBN sample

Monocrystalline hBN was neutron-irradiated in the Triga Mark I IPR-R1 nuclear reactor [Centro de Desenvolvimento da Tecnologia Nuclear (CDTN), Brazil], with a thermal flux of 4×10^{12} n/cm^2 per second for 16 hours reaching an integrated dose of approximately 2.3×10^{18} n/cm^2. For more details about sample preparation by fast neutrons and thermal stability of produced defects, see reference (*47*). The concentration of V_B^- is determined by means of electron paramagnetic resonance without illumination as $N = 5.4 \times 10^{17}$ cm^{-3}, and the concentration of the defects in the sheet can be estimated as 1.8×10^{12} cm^{-2}. For details, see fig. S3.

CW ODMR

All low-field ODMR measurements were performed with a homemade confocal setup. A 532-nm laser (Cobolt Samba 100) was coupled into a 50-μm fiber and focused onto the sample with a 10× objective (Olympus LMPLN10XIR), which excited a voxel in the sample with a diameter of about 10 μm. Because the laser light penetrates the whole crystal, we estimate 2.6×10^9 equally addressed and coherently driven spins. The PL was separated from the laser by a dichroic mirror, and the residual laser light was absorbed by a 532-nm long-pass filter. Afterward, the PL was coupled into a 600-μm fiber and guided to an avalanche photodiode (Thorlabs, APD440A). A 0.5-mm-wide copper stripline was used to apply microwaves to the on-top laying hBN sample. The microwaves were generated by a signal generator (Stanford Research Systems, SG384) and amplified by a Mini Circuits ZVE-3W-83+ amplifier. A lock-in detection was applied (Signal Recovery 7230 lock-in amplifier) using an on-off modulation of the microwaves. For an external magnetic field, a permanent magnet was mounted below the sample.

CW hole-burning ODMR

In addition, to the described CW ODMR setup, a second identical microwave source is added to the first frequency with a combiner (Mini Circuits ZFRSC-183-S+) in front of the amplifier (Mini Circuits ZVE-3W-83+).

Pulsed ODMR

A pulse blaster card (PulseBlasterESR PRO 500 MHz) was used for building the described pulse sequences. The optical excitation is pulsed by an acousto-optic modulator (AOM) (AA.MT250-A0,2-VIS), and the microwave pulses are formed by a fast switching solid-state microwave switch (ZASWA-2-50DR+) directly after the microwave generator. The amplification to the required microwave power is performed by a Vectawave VBA2060-25. For the detection, an avalanche photodiode (APD) with a higher bandwidth was used (Thorlabs, APD120A/M), which is then digitized by a digitizer card (GaGe CompuScope).

SUPPLEMENTARY MATERIALS

Supplementary material for this article is available at http://advances.sciencemag.org/cgi/content/full/7/14/eabf3630/DC1

REFERENCES AND NOTES

1. A. K. Geim, I. V. Grigorieva, Van der Waals heterostructures. *Nature* **499**, 419–425 (2013).
2. K. S. Novoselov, A. Mishchenko, A. Carvalho, A. H. Castro Neto, 2D materials and van der Waals heterostructures. *Science* **353**, aac9439 (2016).
3. W. Ma, P. Alonso-González, S. Li, A. Y. Nikitin, J. Yuan, J. Martín-Sánchez, J. Taboada-Gutiérrez, I. Amenabar, P. Li, S. Vélez, C. Tollan, Z. Dai, Y. Zhang, S. Sriram, K. Kalantar-Zadeh, S. T. Lee, R. Hillenbrand, Q. Bao, In-plane anisotropic and ultra-low-loss polaritons in a natural van der Waals crystal. *Nature* **562**, 557–562 (2018).
4. L. A. Jauregui, A. Y. Joe, K. Pistunova, D. S. Wild, A. A. High, Y. Zhou, G. Scuri, K. De Greve, A. Sushko, C.-H. Yu, T. Taniguchi, K. Watanabe, D. J. Needleman, M. D. Lukin, H. Park, P. Kim, Electrical control of interlayer exciton dynamics in atomically thin heterostructures. *Science* **366**, 870–875 (2019).
5. T. T. Tran, K. Bray, M. J. Ford, M. Toth, I. Aharonovich, Quantum emission from hexagonal boron nitride monolayers. *Nat. Nanotech.* **11**, 37–41 (2016).
6. A. Gottscholl, M. Kianinia, V. Soltamov, S. Orlinskii, G. Mamin, C. Bradac, C. Kasper, K. Krambrock, A. Sperlich, M. Toth, I. Aharonovich, V. Dyakonov, Initialization and read-out of intrinsic spin defects in a van der Waals crystal at room temperature. *Nat. Mater.* **19**, 540–545 (2020).
7. M. Abdi, J.-P. Chou, A. Gali, M. B. Plenio, Color centers in hexagonal boron nitride monolayers: A group theory and ab initio analysis. *ACS Photonics* **55**, 1967–1976 (2018).
8. C. Gong, L. Li, Z. Li, H. Ji, A. Stern, Y. Xia, T. Cao, W. Bao, C. Wang, Y. Wang, Z. Q. Qiu, R. J. Cava, S. G. Louie, J. Xia, X. Zhang, Discovery of intrinsic ferromagnetism in two-dimensional van der Waals crystals. *Nature* **546**, 265–269 (2017).
9. B. Huang, G. Clark, E. Navarro-Moratalla, D. R. Klein, R. Cheng, K. L. Seyler, D. Zhong, E. Schmidgall, M. A. McGuire, D. H. Cobden, W. Yao, D. Xiao, P. Jarillo-Herrero, X. Xu, Layer-dependent ferromagnetism in a van der Waals crystal down to the monolayer limit. *Nature* **546**, 270–273 (2017).
10. H. Li, S. Ruan, Y.-J. Zeng, Intrinsic van der Waals magnetic materials from bulk to the 2D Limit: New frontiers of spintronics. *Adv. Mater.* **31**, 1900065 (2019).
11. S. Liu, K. Yang, W. Liu, E. Zhang, Z. Li, X. Zhang, Z. Liao, W. Zhang, J. Sun, Y. Yang, H. Gao, C. Huang, L. Ai, P. K. J. Wong, A. T. S. Wee, A. T. N'Diaye, S. A. Morton, X. Kou, J. Zou, Y. Xu, H. Wu, F. Xiu, Two-dimensional ferromagnetic superlattices. *Nat. Sci. Rev.* **7**, 745–754 (2020).
12. F. Jelezko, T. Gaebel, I. Popa, A. Gruber, J. Wrachtrup, Observation of coherent oscillations in a single electron spin. *Phys. Rev. Lett.* **92**, 076401 (2004).
13. B. C. Rose, D. Huang, Z.-H. Zhang, P. Stevenson, A. M. Tyryshkin, S. Sangtawesin, S. Srinivasan, L. Loudin, M. L. Markham, A. M. Edmonds, D. J. Twitchen, S. A. Lyon, N. P. de Leon, Observation of an environmentally insensitive solid-state spin defect in diamond. *Science* **361**, 60–63 (2018).
14. W. F. Koehl, B. B. Buckley, F. J. Heremans, G. Calusine, D. D. Awschalom, Room temperature coherent control of defect spin qubits in silicon carbide. *Nature* **479**, 84–87 (2011).
15. R. Kolesov, K. Xia, R. Reuter, M. Jamali, R. Stöhr, T. Inal, P. Siyushev, J. Wrachtrup, Mapping spin coherence of a single rare-earth ion in a crystal onto a single photon polarization state. *Phys. Rev. Lett.* **111**, 120502 (2013).
16. J. M. Kindem, A. Ruskuc, J. G. Bartholomew, J. Rochman, Y. Q. Huan, A. Faraon, Control and single-shot readout of an ion embedded in a nanophotonic cavity. *Nature* **580**, 201–204 (2020).
17. V. Ivády, G. Barcza, G. Thiering, S. Li, H. Hamdi, J.-P. Chou, Ö. Legeza, A. Gali, Ab initio theory of the negatively charged boron vacancy qubit in hexagonal boron nitride. *npj Comput. Mater.* **6**, 41 (2020).
18. A. Jarmola, V. M. Acosta, K. Jensen, S. Chemerisov, D. Budker, Temperature- and magnetic-field-dependent longitudinal spin relaxation in nitrogen-vacancy ensembles in diamond. *Phys. Rev. Lett.* **108**, 197601 (2012).
19. K. H. Michel, B. Verberck, Phonon dispersions and piezoelectricity in bulk and multilayers of hexagonal boron nitride. *Phys. Rev. B* **83**, 115328 (2011).
20. S. Jung, M. Park, J. Park, T.-Y. Jeong, H.-J. Kim, K. Watanabe, T. Taniguchi, D. H. Ha, C. Hwang, Y.-S. Kim, Vibrational properties of *h*-BN and *h*-BN-graphene heterostructures probed by inelastic electron tunneling spectroscopy. *Sci. Rep.* **5**, 16642 (2015).
21. D. Simin, H. Kraus, A. Sperlich, T. Oshima, G. V. Astakov, V. Dyakonov, Locking of electron spin coherence above 20 ms in natural silicon carbide. *Phys. Rev. B* **95**, 161201 (2017).
22. A. Norambuena, E. Muñoz, H. T. Dinani, D. Budker, J. R. Maze, Spin-lattice relaxation of individual solid-state spins. *Phys. Rev. B* **97**, 094304 (2018).
23. E. L. Hahn, Spin echoes. *Phys. Rev.* **80**, 580–594 (1950).
24. R. J. Blume, Electron spin relaxation times in sodium-ammonia solutions. *Phys. Rev.* **109**, 1867–1873 (1958).
25. A. Ponti, A. Schweiger, Echo phenomena in electron paramagnetic resonance spectroscopy. *Appl. Magn. Reson.* **7**, 363–403 (1994).

26. W. G. Breiland, C. B. Harris, A. Pines, Optically detected electron spin echoes and free precession in molecular excited states. *Phys. Rev. Lett.* **30**, 158–161 (1973).
27. W. G. Breiland, H. C. Brenner, C. B. Harris, Coherence in multilevel systems. I. Coherence in excited states and its application to optically detected magnetic resonance in phosphorescent triplet states. *J. Chem. Phys.* **62**, 3458 (1975).
28. C. Kasper, D. Klenkert, Z. Shang, D. Simin, A. Gottscholl, A. Sperlich, H. Kraus, C. Schneider, S. Zhou, M. Trupke, W. Kada, T. Ohshima, V. Dyakonov, G. V. Astakhov, Influence of irradiation on defect spin coherence in silicon carbide. *Phys. Rev. Appl.* **13**, 044054 (2020).
29. W. B. Mims, Envelope modulation in spin-echo experiments. *Phys. Rev. B* **5**, 2409–2419 (1972).
30. V. Weis, K. Möbius, T. Prisner, Optically detected electron spin echo envelope modulation on a photoexcited triplet state in zero magnetic – field a comparison between the zero-field and high-field limits. *J. Magn. Reson.* **131**, 17–24 (1998).
31. L.-P. Yang, C. Burk, M. Widmann, S.-Y. Lee, J. Wrachtrup, N. Zhao, Electron spin decoherence in silicon carbide nuclear spin bath. *Phys. Rev. B* **90**, 241203 (2014).
32. S. Takahashi, R. Hanson, J. van Tol, M. S. Sherwin, D. D. Awschalom, Quenching spin decoherence in diamond through spin bath polarization. *Phys. Rev. Lett.* **101**, 047601 (2008).
33. J. H. Lee, J. J. Song, M. A. F. Scarparo, M. D. Levenson, Coherent population oscillations and hole burning observed in Sm^{+2}:CaF_2 using polarization spectroscopy. *Opt. Lett.* **5**, 196 (1980).
34. L. W. Hillman, R. W. Boyd, J. Krasinski, C. R. Stroud Jr., Observation of a spectral hole due to population oscillations in a homogeneously broadened optical absorption line. *Opt. Commun.* **45**, 416–419 (1983).
35. P. Kehayias, M. Mrózek, V. M. Acosta, A. Jarmola, D. S. Rudnicki, R. Folman, W. Gawlik, D. Budker, Microwave saturation spectroscopy of nitrogen-vacancy ensembles in diamond. *Phys. Rev. B* **89**, 245202 (2014).
36. V. A. Soltamov, C. Kasper, A. V. Poshakinskiy, A. N. Anisimov, E. N. Mokhov, A. Sperlich, S. A. Tarasenko, P. G. Baranov, G. V. Astakhov, V. Dyakonov, Excitation and coherent control of spin qudit modes in silicon carbide at room temperature. *Nat. Commun.* **10**, 1678 (2019).
37. M. Mrozek, A. M. Wojciechowski, D. S. Rudnicki, J. Zachorowski, P. Kehayias, D. Budker, W. Gawlik, Coherent population oscillations with nitrogen-vacancy color centers in diamond. *Phys. Rev. B* **94**, 035204 (2016).
38. J. J. Song, J. H. Lee, M. D. Levenson, Picosecond relaxation measurements by polarization spectroscopy in condensed phases. *Phys. Rev. A* **17**, 1439–1447 (1978).
39. S. Meiboom, D. Gill, Modified spin-echo method for measuring nuclear relaxation times. *Rev. Sci. Instrum.* **29**, 688–691 (1958).
40. L. Childress, M. V. Gurudev Dutt, J. M. Taylor, A. S. Zibrov, F. Jelezko, J. Wrachtrup, P. R. Hemmer, M. D. Lukin, Coherent dynamics of coupled electron and nuclear spin qubits in diamond. *Science* **314**, 281–285 (2006).
41. G. H. Uhrig, Keeping a quantum bit alive by optimized π-pulse sequences. *Phys. Rev. Lett.* **98**, 100504 (2007).
42. S. T. Ochsenbein, D. R. Gamelin, Quantum oscillations in magnetically doped colloidal nanocrystals. *Nat. Nanotechnol.* **6**, 112–115 (2011).
43. M. Kianinia, S. White, J. E. Fröch, C. Bradac, I. Aharonovich, Generation of spin defects in hexagonal boron nitride. *ACS Photonics* **7**, 2147–2152 (2020).
44. J. Rondin, J.-P. Tetienne, T. Hingant, J.-F. Roch, P. Maletinsky, V. Jacques, Magnetometry with nitrogen-vacancy defects in diamond. *Rep. Prog. Phys.* **77**, 056503 (2014).
45. I. Lovchinsky, J. D. Sanchez-Yamagishi, E. K. Urbach, S. Choi, S. Fang, T. I. Andersen, K. Watanabe, T. Taniguchi, A. Bylinskii, E. Kaxiras, P. Kim, H. Park, M. D. Lukin, Magnetic resonance spectroscopy of an atomically thin material using a single-spin qubit. *Science* **355**, 503–507 (2017).
46. X. Lu, X. Chen, S. Dubey, Q. Yao, W. Li, X. Wang, Q. Xiong, A. Srivastava, Optical initialization of a single spin-valley in charged WSe_2 quantum dots. *Nat. Nanotechnol.* **14**, 426–431 (2019).
47. J. R. Toledo, D. B. de Jesus, M. Kianinia, A. S. Leal, C. Fantini, L. A. Cury, G. A. M. Sáfar, I. Aharonovich, K. Krambrock, Electron paramagnetic resonance signature of point defects in neutron-irradiated hexagonal boron nitride. *Phys. Rev. B* **98**, 155203 (2018).

Acknowledgments: We thank D. Krauße for experimental help with the dark electron paramagnetic resonance measurements. **Funding:** A.G., A.S., and V.D. acknowledge financial support from the DFG through the Würzburg-Dresden Cluster of Excellence on Complexity and Topology in Quantum Matter—ct.qmat (EXC 2147, project-id 39085490) and DY18/13-1.V.S. acknowledges the financial support of the Alexander von Humboldt (AvH) Foundation. The Australian Research "Council (via DP180100077 and CE200100010)" and the Asian Office of Aerospace Research and Development grant (FA2386-20-1-4014) are acknowledged. I.A. is grateful for the Humboldt Foundation for support. **Author contributions:** A.G., M.D., C.K., V.S., and A.S implemented the experimental setups and performed the CW, hole-burning, and pulsed ODMR measurements. I.A., M.K., and C.B. assisted with sample fabrication. V.D. and I.A. conceived and supervised the project. All the authors contributed to the analysis of the data and discussions and to the writing of the paper. **Competing interests:** The authors declare that they have no competing interests. **Data and materials availability:** All data needed to evaluate the conclusions in the paper are present in the paper and the Supplementary Materials at the journal. Additional data related to this paper may be requested from the authors.

Submitted 23 October 2020
Accepted 12 February 2021
Published 2 April 2021
10.1126/sciadv.abf3630

Citation: A. Gottscholl, M. Diez, V. Soltamov, C. Kasper, A. Sperlich, M. Kianinia, C. Bradac, I. Aharonovich, V. Dyakonov, Room temperature coherent control of spin defects in hexagonal boron nitride. *Sci. Adv.* **7**, eabf3630 (2021).

ScienceAdvances

Room temperature coherent control of spin defects in hexagonal boron nitride

Andreas GottscholMatthias DiezVictor SoltamovChristian KasperAndreas SperlichMehran KianiniaCarlo BradacIgor AharonovichVladimir Dyakonov

Sci. Adv., 7 (14), eabf3630. • DOI: 10.1126/sciadv.abf3630

Science Advances (ISSN 2375-2548) is published by the American Association for the Advancement of Science. 1200 New York Avenue NW, Washington, DC 20005. The title *Science Advances* is a registered trademark of AAAS.